Hindawi Publishing Corporation
International Journal of Aerospace Engineering
Volume 2010, Article ID 364859, 11 pages
doi:10.1155/2010/364859

Research Article

Computational Study on Effect of Synthetic Jet Design Parameters

Koichi Okada,[1] Akira Oyama,[2] Kozo Fujii,[2] and Koji Miyaji[1]

[1] *Department of Ocean and Space Engineering, Yokohama National University, Yokohama, Kanagawa 240-8501, Japan*
[2] *Department of Space Transportation Engineering, Institute of Space and Astronautical Science, Japan Aerospace Exploration Agency, Sagamihara, Kanagawa 252-5210, Japan*

Correspondence should be addressed to Koichi Okada, okada@flab.isas.jaxa.jp

Received 2 December 2009; Accepted 29 June 2010

Academic Editor: Mark Price

Effects of amplitude and frequency of synthetic jet on the characteristics of induced jet are investigated. To estimate effects of the parameters, flow inside the synthetic jet cavity and orifice and the outer flow is simultaneously simulated using large-eddy simulation (LES). Comparison of the present LES result with the experimental data shows that three-dimensional LES of the flow inside the cavity is essential for accurate estimation of the velocity and velocity fluctuation of the synthetic jet. Comparison of the present results under various flow conditions shows that amplitude and frequency can control profiles of time-averaged vertical velocity and fluctuation of the vertical velocity as well as damping rate of the induced velocity and fluctuation.

1. Introduction

In recent years, active flow control using microdevices receives people's attention. One type of such flow control devices is called "synthetic jet," which consists of an orifice connected to a cavity, the bottom of which oscillates with small amplitude, produces weak and periodic flow from the orifice [1]. Reference [2] reported that flow separation over a wing can be controlled by inducing weak and periodic flow from its orifice exit. One of the advantages of the synthetic jet over conventional flow control devises is active flow control capability because it can control the induced flow electrically. Another advantage of the synthetic jet is its light weight and compactness as it does not require any air-supplier system. Due to these advantages, synthetic jet is considered to be suitable to various kinds of aircrafts, especially to unmanned air vehicles, micro-air vehicles, and rotorcrafts.

To date, applications of the synthetic jet, however, is limited to control of low-speed flows over a small object (i.e., low Reynolds number flow). The main reason for the limitation is that flow mechanism of the synthetic jet is not well understood, and therefore how to optimize the design parameters, such as amplitude, frequency, and depth of the cavity, is not well known. To make this technology feasible, it is important to understand the flow control mechanism of the synthetic jet and effects of the design parameters.

Actually, many researchers studied characteristics of the flow induced by the synthetic jet [1–5]. Pioneering work was done by Smith and Glezer [1]. They have experimentally studied the characteristics such as velocity distributions, power spectra of the streamwise velocity, and behavior of the vortices (based on Schlieren images). One of the features they found was that vortices created at the orifice exit induce time-averaged vertical velocity that is similar to that of steady turbulent jets. They also demonstrated capability of a simple synthetic jet with high aspect ratio orifice for thrust vectoring.

Kral et al. [5] carried out the computation and compared the results with those of Smith and Glezer [1] and found that Reynolds-averaged Navier-Stokes (RANS) computation by using synthetic jet model based on top-hat type velocity boundary condition agrees with the experiment in terms of the time-averaged vertical velocity distribution of the induced jet. They also found that the data based on RANS computation do not agree well with the experimental data in terms of vertical velocity fluctuation.

Two years after the publication of the work of Kral et al., Rizzetta et al. [6] investigated synthetic jet flowfield with the direct simulation of Navier-stokes equations. They discussed the effects of the Reynolds number of the jet and depth of the cavity on the characteristics of the jet using two-dimensional computation. However, the effect of Reynolds number is

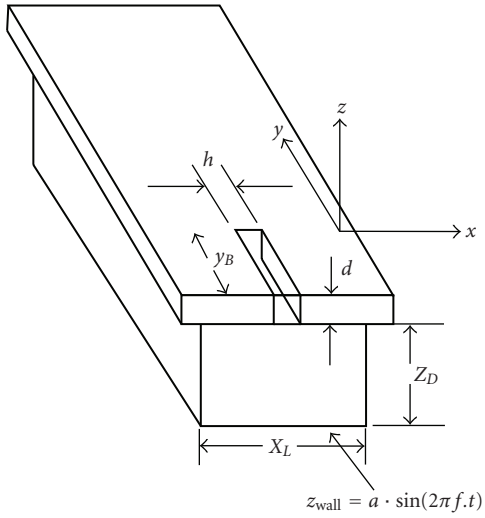

Figure 1: Present synthetic jet configuration [6].

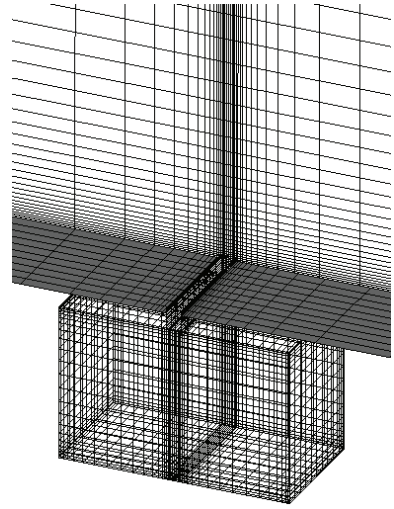

Figure 2: The present computational grids.

not observed in their computation results because they use the two-dimensional computation. They demonstrated one three-dimensional unsteady computation, but the result does not agree with the data of the experiments qualitatively in terms of both time-averaged velocity profiles and fluctuating velocity profiles. The reason for this discrepancy may be that the induced jet is modeled by a boundary condition given at the orifice exit without solving flow inside the cavity.

The synthetic jet has various design parameters: frequency, amplitude, cavity configuration, aspect ratio of the orifice, and so forth. In the present study, effects of input design parameters (frequency and amplitude) on a synthetic jet with a given cavity and orifice geometry are investigated. Three-dimensional flow inside the synthetic jet cavity and orifice and the outer flow is together simulated using large-eddy simulation (LES) for accurate simulation of the synthetic jet.

2. Configuration and Motion of the Synthetic Jet

The geometric configuration of the synthetic jet of reference [6] is chosen for this study (Figure 1). A Cartesian coordinate system is oriented with its origin at the center of the orifice exit. All variables are normalized by the orifice width h. The nondimensional orifice depth d and the nondimensional orifice width h are 1. The cavity depth Z_D is 10 and the cavity width X_L is 15. The cavity span length in the y-direction is treated as infinite in the simulation since that of the experiment is 150 and the edge effect can be ignored near the center of the jet.

The bottom of the cavity is assumed to be a flat plate and the oscillation of the cavity bottom is defined by

$$z_{\text{wall}} = a \cdot \sin(2\pi f \cdot t). \tag{1}$$

Nondimensional numbers in the present study are defined by

$$\text{Mach} = \frac{U_{\text{ref}}}{c}, \tag{2}$$

$$\text{Re} = \frac{U_{\text{ref}} h}{\nu}, \tag{3}$$

$$\text{St} = \frac{f \cdot h}{U_{\text{ref}}}, \tag{4}$$

The reference velocity U_{ref} is defined based on a representative value of the fluctuating velocity at the nozzle exit. Note that the definition of U_{ref} is different for Sections 4 and 5. Details are explained in each section.

3. Computational Approach

3.1. Numerical Method. Three-dimensional compressible Navier-Stokes equations are employed as the governing equations. These equations are solved in the generalized curvilinear coordinates systems. The equations are nondimensionalized based on the orifice width, speed of sound, and ambient density. The spatial derivatives of convective terms and viscous terms, metrics, and Jacobin are evaluated by the sixth-order compact difference scheme [7]. The tenth-order filtering [8] is used with filtering coefficient of 0.45. Deforming and moving grids are used for the metrics and Jacobin computation to satisfy the geometric conservation law [9]. For time integration, Alternating Direction Implicit-Symmetric Gauss-Seidel (ADI-SGS) implicit method with three subiterations (Newton-Rhaphson iterations) [10] in each time step is adopted. This algorithm uses same kind of idea of Four-Factored Symmetric Gauss-Seidel (FF-SGS) [11] which adopts both ideas of the Lower-Upper Symmetric Alternating Direction Implicit (LU-ADI) and the Lower-Upper Symmetric Gauss-Seidel (LU-SGS). Second-order

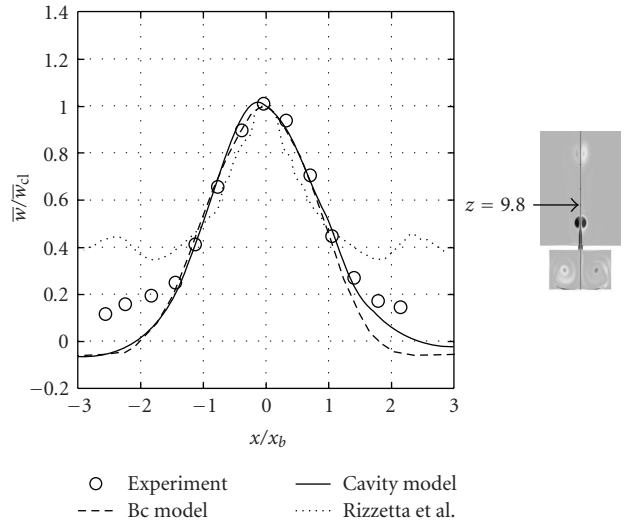

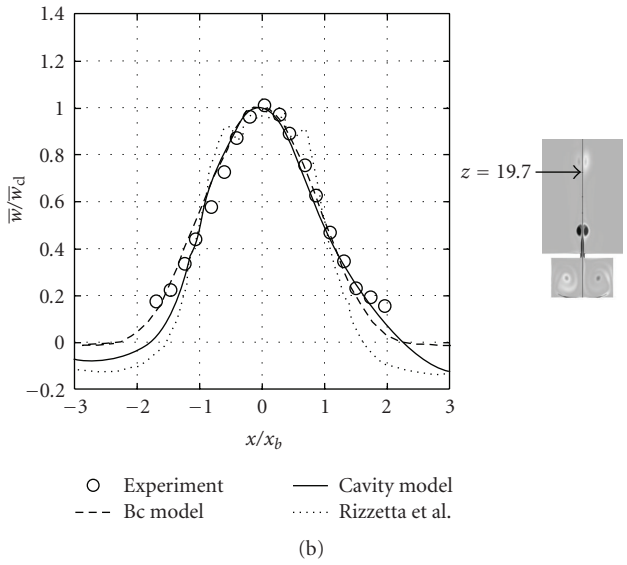

Figure 3: Comparison of the time-averaged velocity distributions between the computational results and the experimental result.

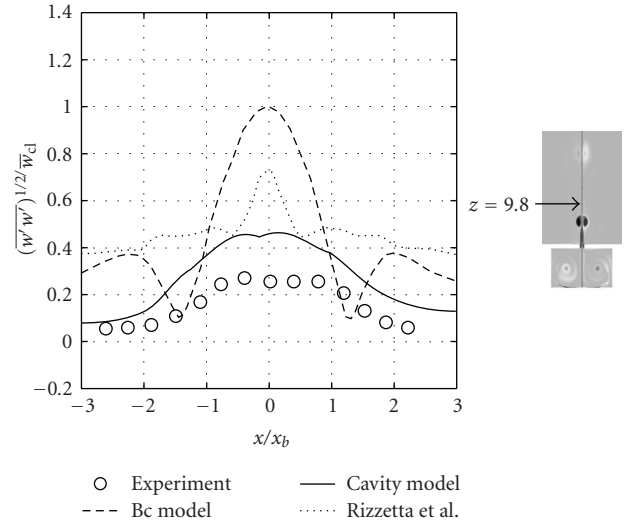

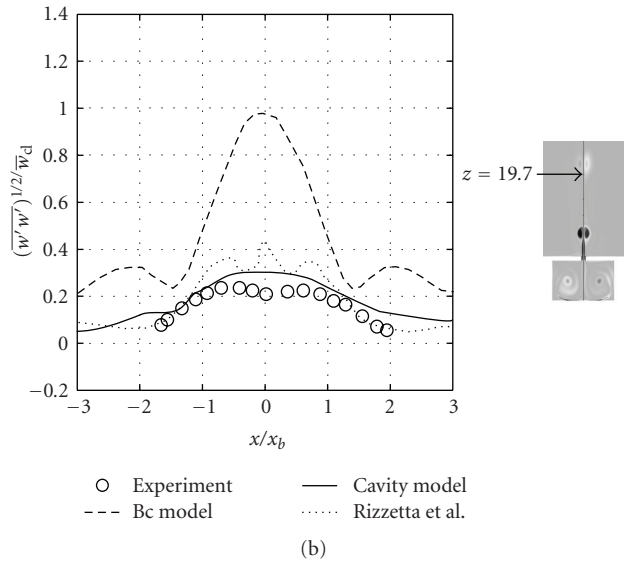

Figure 4: Comparison of distributions of the RMS value of vertical velocity fluctuation component between the computational results and the experimental result.

temporal accuracy is guaranteed by a three-level backward-differencing formula. The computational time step is 0.02 in the nondimensional time so that the maximum Courant-Friedrichs-Levy number becomes approximately 1.0. Turbulence model is not used because of the small Reynolds number (Re = 338–1345).

3.2. Computational Grids. Zonal grid approach [12] is employed to generate grids for cavity, orifice, and external regions as shown in Figure 2. The grid points show every five points in each direction. The grid deformation approach developed by Melville et al. [13] is applied to generate a time-varying fluid grid system for the cavity region. This algebraic method can maintain the grid quality of the initial grid near the deforming surfaces under arbitrary, moderate deflections and rotations. The total number of the grid points is approximately 3,200,000 (see Table 1). Note that spatial resolution of sixth-order compact difference scheme is in general much finer than conventional second-order scheme in each direction. Our experience indicates that the

Table 1: Number of the grid points of the current computational grids.

	Grid
	$X \times Y \times Z$
Zone 1: cavity region	$199 \times 51 \times 105$
Zone 2: orifice region	$51 \times 51 \times 67$
Zone 3: external region	$233 \times 51 \times 211$

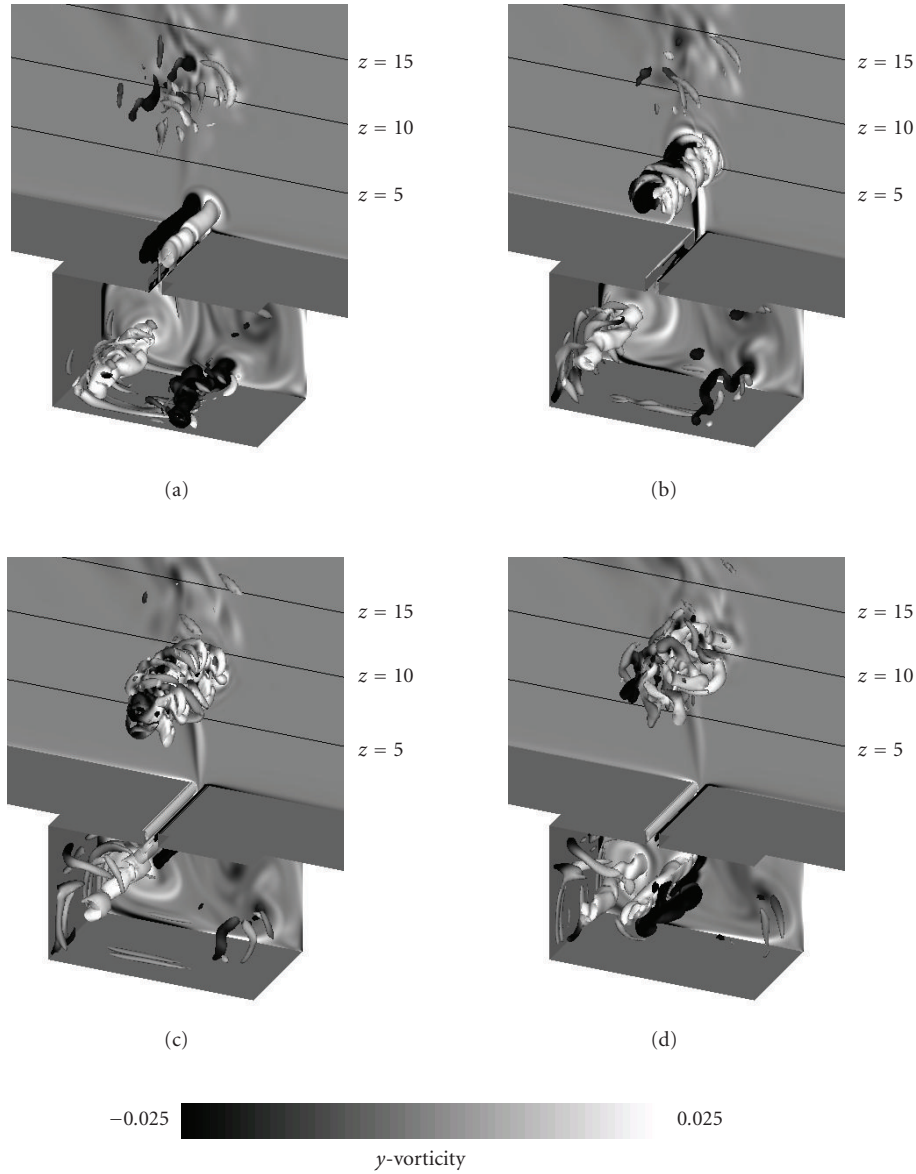

Figure 5: Instantaneous Q isosurfaces of Case 1 (low frequency case). (Isosurfaces are colored with y-vorticity).

Table 2: Computational conditions for comparison with experimental data [1].

Mach	Re	St
0.065	750	0.027

results by the present method would correspond to that by the conventional method with 50 to 100 times more grid points. Between each region, six grid points are overlapped to maintain the same accuracy as the internal grid points. The minimum grid size in each direction of all grids is $dx = 0.02$, $dy = 0.16$, and $dz = 0.02$. The outer boundary is located at 1000 d away from the orifice exit. The length of the computational region in span direction (y-direction) is 8 d and periodic boundary condition is applied to the spanwise boundaries.

4. Comparison with Experimental Data

In this section, the present result is compared with the experimental data [1] for validation purpose. The synthetic jet device in reference [1] forms the jet normal to a flat plate of 30 × 38 cm at a rectangular orifice measuring 0.5 × 75 mm under static air condition. The Reynolds number of the jet, defined based on the orifice width and the range of amplitudes of the nominally time-harmonic streamwise velocity, is between 500 and 1000.

Flow conditions of the present computations follow the above experimental conditions. Table 2 shows the nondimensional numbers of the present computation where the nondimensional numbers are defined by (2)–(4) and U_{ref} is the measured maximum vertical velocity at the center of the orifice exit. In the present LES, the amplitude of the synthetic jet oscillation is set to 0.41, which gives us the same value of

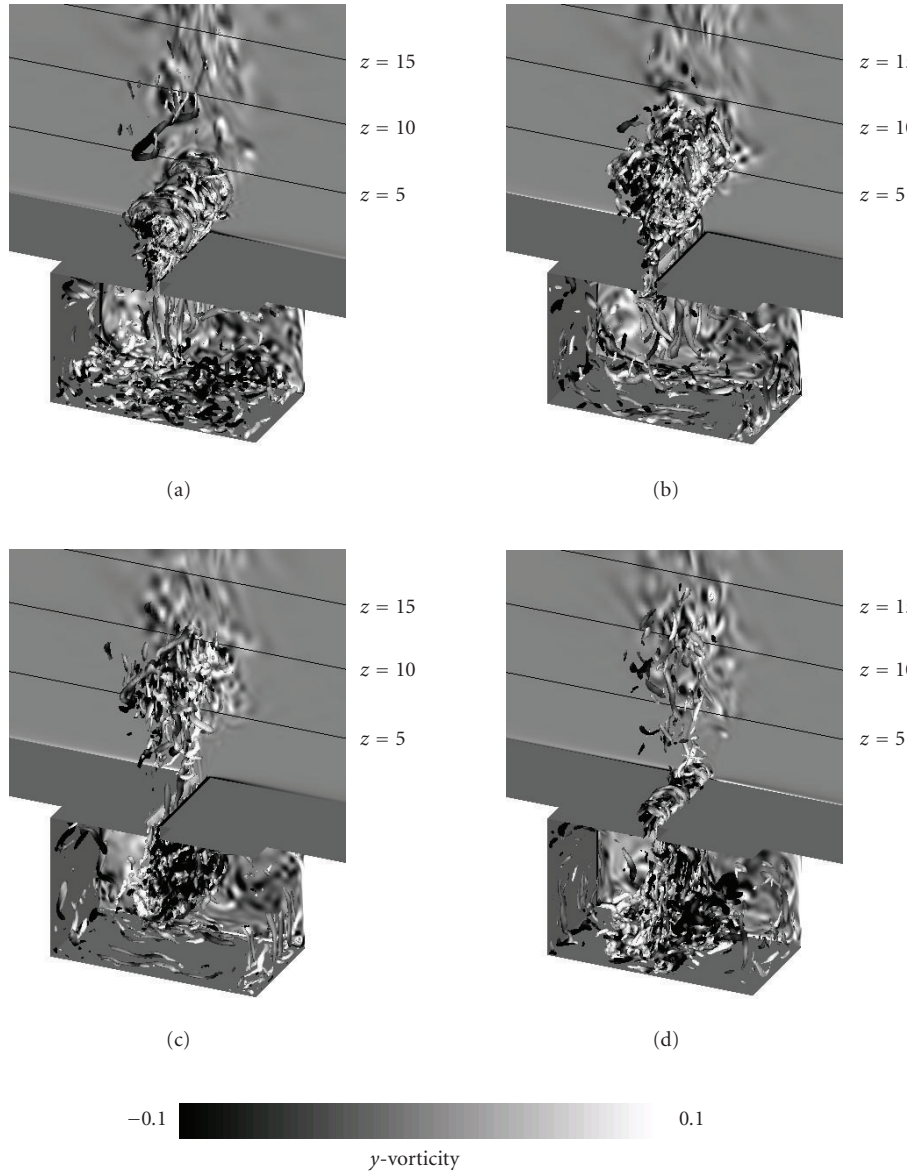

Figure 6: Instantaneous Q isosurfaces of Case 2 (high frequency case).

maximum vertical velocity at the center of the orifice exit as that in the referenced experiment. The present result is also compared with LES result where the synthetic jet is given at the orifice exit and the flow inside cavity is not solved. Vertical velocity at the orifice exit is defined by the following equation:

$$U_{\text{jet}} = g \cdot \sin(2\pi f \cdot t), \tag{5}$$

where the nondimensional amplitude of the jet velocity g is set to a constant value of 0.065, which corresponds to the maximum velocity at the orifice exit of the reference experiment. U_{jet} is a constant value for x-direction due to g being the constant value. The nondimensional frequency of the jet velocity is set to 0.027, which corresponds to the reference experiment.

Figures 3 and 4 compare the distributions of the time-averaged vertical velocity and root mean square (RMS) values of the vertical velocity fluctuation component, respectively. As presented in reference [1], the vertical velocity and the fluctuation is normalized with time-averaged velocity at the center of the orifice exit of each case. The horizontal axis is also normalized by jet half-width x_b, which is x-coordinate of the position where the vertical velocity becomes half value of the maximum vertical velocity (as a result, the normalized vertical velocity becomes 0.5 at $x/x_b = \pm 1.0$).

Four results are presented; (1) the present LES with the flow inside the cavity solved (denoted by Cavity model), (2) the present LES with the boundary condition given by (5) instead of LES of flow inside the cavity (denoted by Bc model), (3) Computational result of Rizzetta et al. [6], and (4) the reference experiment (denoted by experiment).

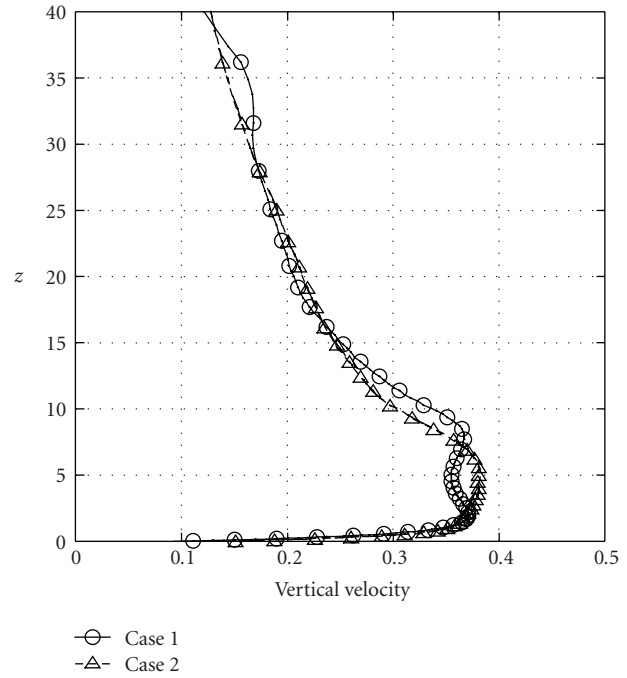

Figure 7: Comparison of distributions of the time averaged velocity of Case 1 (low frequency) and Case 2 (high frequency) at the center of the orifice exit.

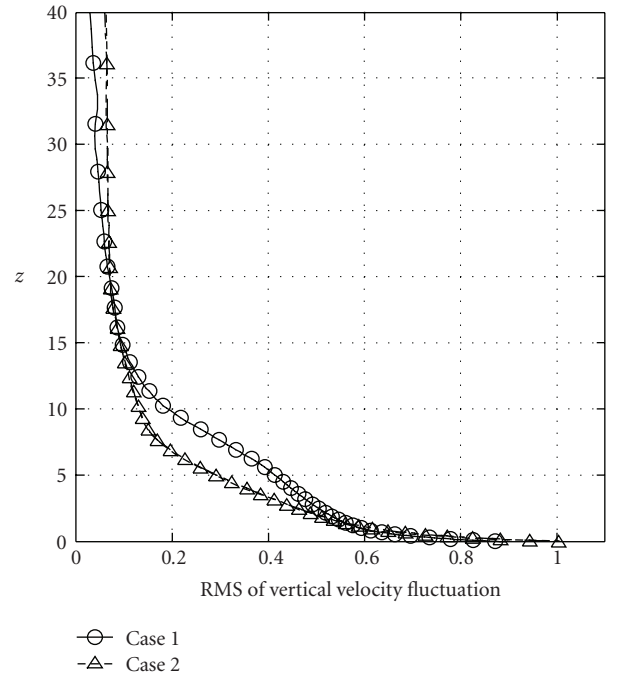

Figure 8: Comparison of distributions of the RMS value of vertical velocity fluctuation component of Case 1 (low frequency) and Case 2 (high frequency) at the center of the orifice exit.

The results are compared at $z = 9.8$ and 19.7. It should be noted that computational approach of Rizzetta et al. is different from our approach in the sense that (1) because the cavity span length is finite (=10), effects of the ends of the orifice are not negligible, (2) only one-quarter of the flow field is solved (symmetric boundary conditions are given at $x = 0$ and $y = 0$), and (3) flow inside the cavity is not solved (instead, the flow at the orifice exit is given by recorded data of two-dimensional unsteady synthetic jet flow computation that is obtained before LES).

These figures show that the results of the vertical velocity and fluctuation of current computation solving the three-dimensional flow inside the cavity agree well with the experimental data quantitatively and qualitatively, respectively. Difference in the fluctuation may be due to the difference in the geometry of the synthetic jet as the detail of the synthetic jet geometry used in the experiment is not shown in the reference for the proprietary reason.

Vertical velocity distribution of the current LES with synthetic jet given by the boundary condition also agrees well with the experimental data qualitatively. However, RMS value of vertical velocity fluctuation is overestimated compared with Cavity model. This is because the boundary condition given by (5) produces a pair of very strong y-directional vortices.

The computation of Rizzetta et al. does not agree well with the experiment. According to the result presented in their article, the induced jet simulated by their approach also involves very strong y-directional vortices, which is probably due to the result of the two-dimensional computation inside the cavity. These vortices probably contribute to the overestimated fluctuation at $z = 9.8$. Difference in the geometry (span of the orifice is finite in their computation) and symmetric boundary conditions are also the reasons for the discrepancy. These results indicate that LES of the flow inside the cavity is essential to estimate the velocity and velocity fluctuation of the induced jet.

5. Effect of Design Parameters on the Synthetic Jet

To discuss effect of frequency and amplitude on the synthetic jet, LES is conducted in some conditions presented in Table 3. These parameter ranges are defined according to the synthetic jet parameter ranges in [2].

5.1. Relation between the Design Variables and the Nondimensional Parameters. Before effect of frequency and amplitude on the synthetic jet is discussed, relation between the design parameters and nondimensional parameters are examined. Here, the reference velocity is the maximum value of the spatially-averaged vertical velocity at the orifice exit. From (1), the velocity of the cavity wall is obtained as

$$U_{\text{wall}} = \frac{dz_{\text{wall}}}{dt} = 2\pi f \cdot a \cdot \cos(2\pi f t). \tag{6}$$

When incompressible flow is assumed, the mass flow of the

Table 3: Computational conditions of all cases.

	Oscillation parameters		Flow parameters	
Case	Frequency	Amplitude	Re	St
Case 1	500 Hz	0.41	338	0.03
Case 2	2000 Hz	0.41	1345	0.03
Case 3	1000 Hz	0.205	338	0.06
Case 4	1000 Hz	0.82	1345	0.015

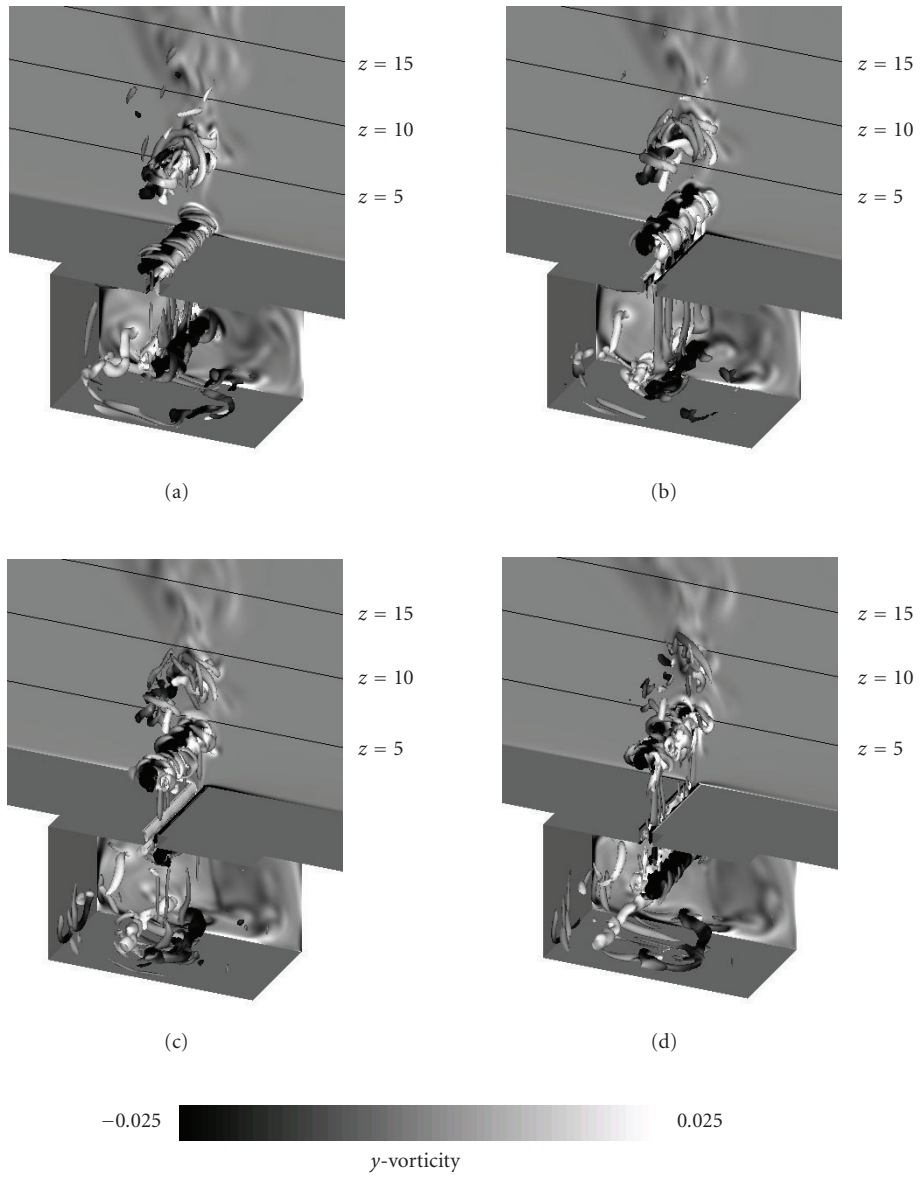

Figure 9: Instantaneous Q isosurfaces of Case 3 (low amplitude case).

orifice exit is equal to the volume change ratio of the cavity. This equation indicates that the peak value of the spatially-averaged vertical velocity is proportional to the frequency and amplitude of the wall motion,

$$U_{\text{ref}} \propto \max_t(U_{\text{wall}}). \tag{7}$$

Because the reference velocity linearly changes as the amplitude and/or frequency change, nondimensional numbers become linear functions of the amplitude and frequency of the oscillation. Equations (3) and (4) and the relation (7) lead to the following relations between the design parameters and nondimensional numbers:

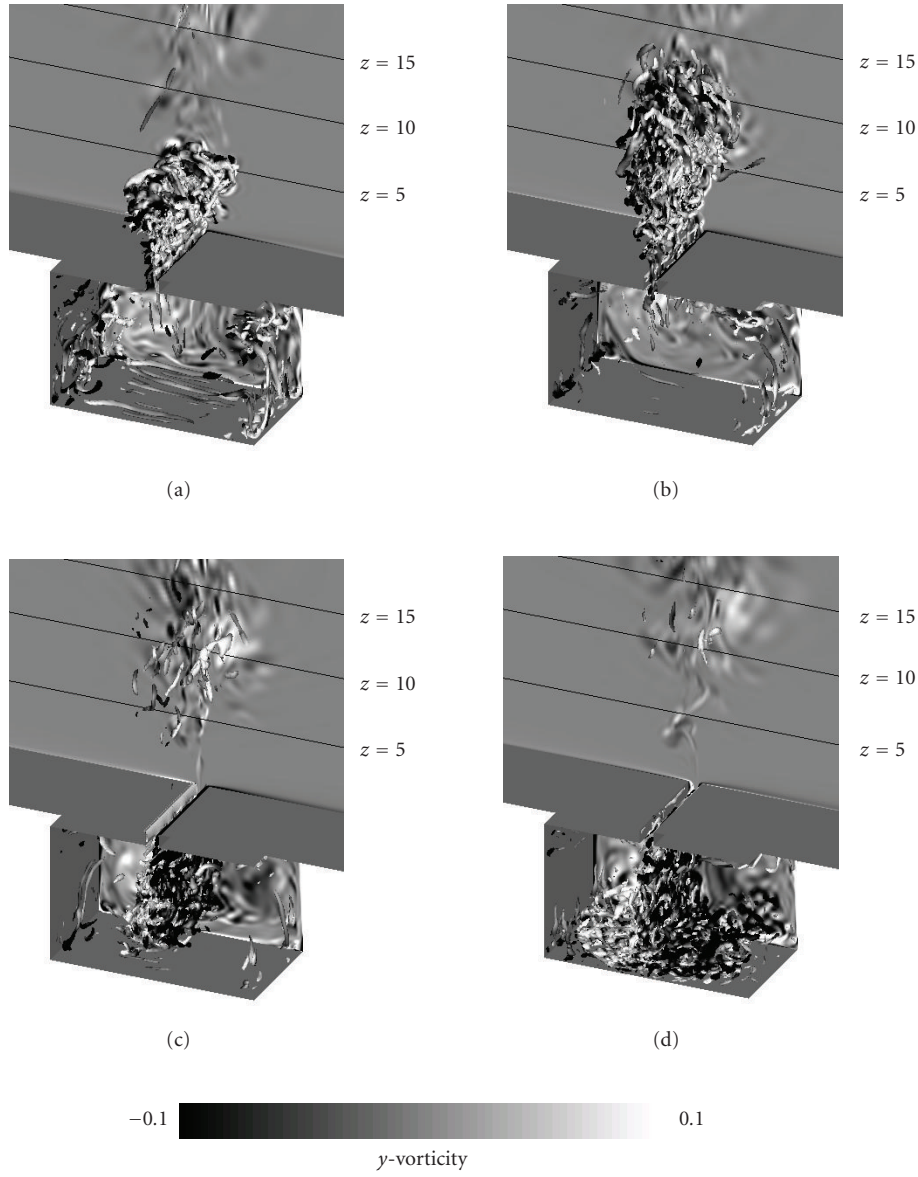

Figure 10: Instantaneous Q isosurfaces of Case 4 (high amplitude case).

$$\mathrm{Re} = \frac{U_{\mathrm{ref}} h}{\nu} \propto fa,$$
$$\mathrm{St} = \frac{f \cdot h}{U_{\mathrm{ref}}} = \frac{f \cdot h}{kfa} \propto \frac{1}{a}. \tag{8}$$

The above analysis gives relation between the design parameters and nondimensional numbers.

(1) As the amplitude increases

(a) spatially-averaged vertical velocity increases,
(b) Reynolds number increases,
(c) Strouhal number decreases,

(2) As the frequency increases

(a) spatially-averaged vertical velocity increases,
(b) Reynolds number increases.

5.2. Effects of Frequency. Results of Case 1 (low frequency) and Case 2 (high frequency) in Table 3 are compared to investigate the effect of frequency on the characteristics of the induced flow. Figure 5 shows instantaneous Q isosurfaces of the computational results of Case 1 (low frequency). The isosurfaces and y-plane at the end of the computational region in the spanwise direction are gray-scaled by y-directional vorticity where white and black regions, respectively, show clockwise and counter-clockwise rotating vortices in the y-direction. Figures 5(a) to 5(d) correspond to the conditions when (a) the vertical flow velocity at the orifice exit is maximum (emission), (b) vertical flow velocity is zero (between (a) and (c)), (c) vertical flow velocity is minimum (suction), and (d) vertical velocity is zero (between (c) and (a)).

This figure shows that a pair of counter-rotating two-dimensional y-directional vortices is emitted from the orifice

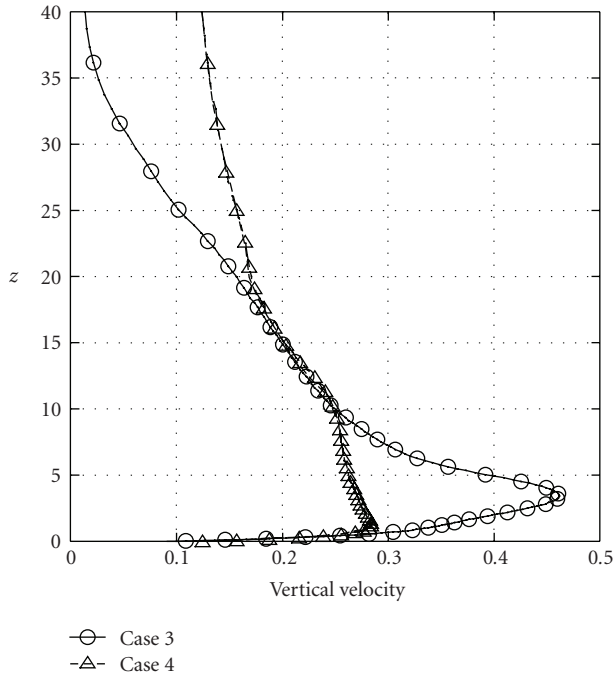

Figure 11: Comparison of distributions of the time averaged velocity of Case 3 (low amplitude) and Case 4 (high amplitude) at the center of the orifice exit.

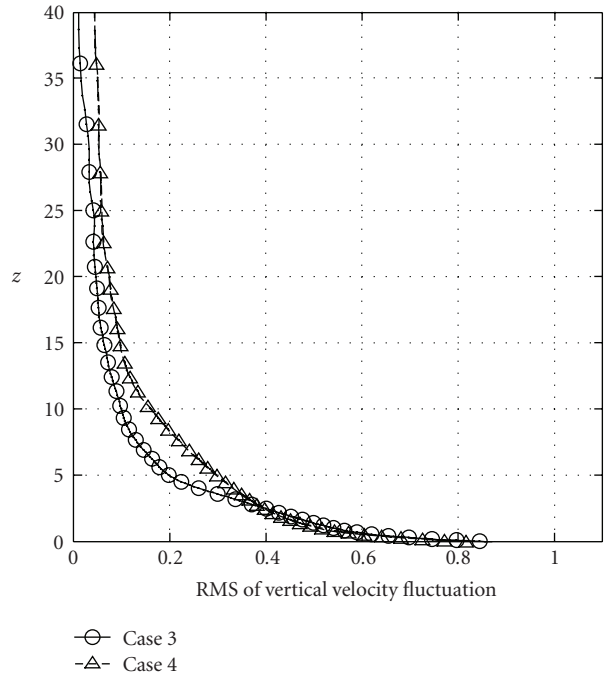

Figure 12: Comparison of distributions of the RMS value of vertical velocity fluctuation component of Case 3 (low amplitude) and Case 4 (high amplitude) at the center of the orifice exit.

exit (see Figure 5(a)). The pair of counter-rotating two-dimensional y-directional vortices with a few longitudinal vortices in the x-direction is propagated in vertical direction (see Figure 5(b)). Due to the longitudinal vortices, structure of the pair of the strong y-directional vortices is destroyed from $z = 10.0$ to 15.0 (see Figures 5(a) to 5(d)) and a pair of strong y-directional vortices are formed inside the cavity (see Figure 5(c)) and then mildly three-dimensional flow structure is formulated (see Figure 5(d)).

Figure 6 is an instantaneous Q isosurfaces of the result of Case 2 (high frequency). A pair of counter-rotating y-directional vortices with numberless longitudinal vortices in the x-direction is emitted from the orifice exit (see Figure 6(a)). Due to the longitudinal vortices, structure of the pair of the strong y-directional vortices is destroyed before it reaches $z = 10$ (see Figures 6(b) to 6(d)). A pair of strong y-directional vortices with longitudinal vortices is formed inside the cavity (see Figure 6(c)) and then highly three-dimensional flow structure is formulated (see Figure 6(d)). This observation also indicates that depth of the cavity may be one of the important design parameters of the synthetic jet.

Figures 7 and 8 compare distributions of the time-averaged values of vertical velocity and the RMS values of vertical velocity fluctuation component at the center of the orifice exit, respectively, where these values are normalized by the reference velocity of each case. In Case 1 (low frequency), the vertical velocity decreases monotonically from roughly $z = 8.0$. In Case 2 (high frequency), the vertical velocity start to decrease at $z = 5.0$ and velocity fluctuation start to decrease at $z = 0.0$ because the pair of the strong y-directional vortices involves much longitudinal vortices.

5.3. Effects of Amplitude. To discuss effects of amplitude on the characteristics of the induced flow, computational results of Case 3 (low amplitude) and Case 4 (high amplitude) shown in Table 3 are compared. Instantaneous Q isosurfaces of Case 3 (low amplitude) and Case 4 (high amplitude) are shown in Figures 9 and 10. In Case 3 (low amplitude), induced vortices strongly interact with other vortices produced in previous cycles both inside and outside the cavity because of high Strouhal number (see B) to (D)). In Case 4 (high amplitude), finer three-dimensional vortex structure due to the increase in Reynolds number is generated while less interaction between vortices is observed due to low Strouhal number.

Time-averaged values vertical velocity and the RMS values of the vertical velocity fluctuation component at the center of the orifice exit are compared in Figures 11 and 12, respectively, where these values are normalized by the reference velocity of each case. In Case 3 (low amplitude), the vertical velocity decrease at $z = 4.0$ and velocity fluctuation decrease at $z = 0.0$ due to the interaction of vortices. In Case 4 (high amplitude), the damping ratio of the vertical velocity and velocity fluctuation moderate compared with Case 3 (low amplitude) because the interaction is weak.

6. Summary

Effects of frequency and amplitude on characteristics of synthetic jet are investigated. To accurately simulate the synthetic jet, flow inside the synthetic jet cavity and orifice and the outer flow is simulated using LES.

Comparison of the present LES result with the experimental data shows that three-dimensional LES of the flow inside the cavity is essential for accurate estimation of the velocity and velocity fluctuation of the synthetic jet. This indicates that three-dimensional vortex structure created inside the cavity probably play important role in flow control with synthetic jet.

Comparison of the present LES results in different frequency conditions shows that the induced jet and the flow inside the cavity have highly three-dimensional vortex structure in high-frequency flow condition due to increase in Reynolds number. As a result, there is a significant difference in the damping rate of time-averaged vertical velocity and the velocity fluctuation.

To discuss amplitude effects, the LES results in different amplitude flow conditions are compared. The present results show that induced vortices strongly interact with other vortices produced in previous cycles both inside and outside the cavity in low-amplitude condition due to high Strouhal number. The present results also show that the induced jet has coarser vortex structure in low-amplitude condition due to low Reynolds number. As a result, time-averaged velocity and velocity fluctuation diffuses faster in low-amplitude case.

Nomenclature

a: Dimensional amplitude of cavity wall oscillation
c: Sound of speed
d: Nondimensional orifice depth
dx: Computational grid spacing in x-direction
dy: Computational grid spacing in y-direction
dz: Computational grid spacing in z-direction
f: Dimensional frequency of jet
g: Amplitude of jet modeled by boundary condition
h: Nondimensional orifice width
Mach: Mach number
ν: Viscosity
Re: Reynolds number
St: Strouhal number
Q: Second invariant of the velocity gradient tensor
t: Time
U_{jet}: Velocity at the orifice exit of jet modeled by boundary condition
U_{ref}: Reference velocity
U_{wall}: Velocity of the bottom of cavity
w: Nondimensional Cartesian velocity component in z-direction
w': Fluctuation velocity component in z-direction
w_{cl}: Nondimensional Cartesian velocity component in z-direction at the centerline
X_L: Nondimensional cavity width
x: Nondimensional Cartesian coordinate in transverse direction
x_b: Cross-stream jet half-width
y: Nondimensional Cartesian coordinate in spanwise direction
y_B: Nondimensional orifice half span
z: Nondimensional Cartesian coordinate in streamwise direction
Z_D: Nondimensional cavity depth.

Superscript

$\overline{\cdot}$: Time-averaged quantity.

Acknowledgment

This work is partially supported by Grant-in-Aid for Scientific Research 20246122.

References

[1] B. L. Smith and A. Glezer, "Vectoring and small-scale motions effected in free shear flows using synthetic jet actuators," in *Proceedings of the 35th AIAA Aerospace Sciences Meeting*, 1997, AIAA Paper no. 1997-0213.

[2] A. Glezer, M. Amitay, and A. M. Honohan, "Aspects of low- and high-frequency actuation for aerodynamic flow control," *AIAA Journal*, vol. 43, no. 7, pp. 1501–1511, 2005.

[3] M. Amitay, D. R. Smith, V. Kibens, D. E. Parekh, and A. Glezer, "Aerodynamic flow control over an unconventional airfoil using synthetic jet actuators," *AIAA Journal*, vol. 39, no. 3, pp. 361–370, 2001.

[4] S. G. Mallinson, G. Hong, and J. A. Reizes, "Some characteristics of synthetic jets," in *Proceedings of the AIAA Computational Fluid Dynamics Conference*, 1999, AIAA Paper no. 1999-3651.

[5] L. D. Kral, J. F. Donovan, A. B. Cain, and A. W. Cary, "Numerical simulation of synthetic jet actuators," in *Proceedings of the AIAA 28th Fluid Dynamics Conference*, 1997, Paper no. 1997-1824.

[6] D. P. Rizzetta, M. R. Visbal, and M. J. Stanek, "Numerical investigation of synthetic-jet flow fields," *AIAA Journal*, vol. 37, no. 8, pp. 919–927, 1999.

[7] S. K. Lele, "Compact finite difference schemes with spectral-like resolution," *Journal of Computational Physics*, vol. 103, no. 1, pp. 16–42, 1992.

[8] D. V. Gaitonde and M. R. Visbal, "Padé-type higher-order boundary filters for the Navier-Stokes equations," *AIAA Journal*, vol. 38, no. 11, pp. 2103–2112, 2000.

[9] M. R. Visbal and R. E. Gordnier, "A higher-order flow solver for deforming and moving meshes," in *Proceedings of the AIAA Aerospace Sciences Meeting*, 2000, AIAA Paper no. 2000-2619.

[10] S. R. Chakravarthy, "Relaxation methods for unfactored implicit upwind schemes," in *Proceedings of the 39th AIAA Aerospace Sciences Meeting*, 1984, AIAA Paper no. 1984-0165.

[11] K. Fujii, "Efficiency improvement of unified implicit relaxation/time integration algorithms," *AIAA Journal*, vol. 37, no. 1, pp. 125–128, 1999.

[12] K. Fujii, "Unified zonal method based on the fortified solution algorithm," *Journal of Computational Physics*, vol. 118, no. 1, pp. 92–108, 1995.

[13] R. B. Melville, S. A. Morton, and D. P. Rizzetta, "Implementation of a fully-implicit, aeroelastic Navier-Stokes solver," in *Proceedings of the Proceedings of the AIAA Aerospace Sciences Meeting*, 1997, AIAA Paper no. 1997-2039.